

Soft Matter

Accepted Manuscript



This is an *Accepted Manuscript*, which has been through the Royal Society of Chemistry peer review process and has been accepted for publication.

Accepted Manuscripts are published online shortly after acceptance, before technical editing, formatting and proof reading. Using this free service, authors can make their results available to the community, in citable form, before we publish the edited article. We will replace this *Accepted Manuscript* with the edited and formatted *Advance Article* as soon as it is available.

You can find more information about *Accepted Manuscripts* in the [Information for Authors](#).

Please note that technical editing may introduce minor changes to the text and/or graphics, which may alter content. The journal's standard [Terms & Conditions](#) and the [Ethical guidelines](#) still apply. In no event shall the Royal Society of Chemistry be held responsible for any errors or omissions in this *Accepted Manuscript* or any consequences arising from the use of any information it contains.

Evidence of viscoplastic behavior of exfoliated graphite nanofluids[†]

Carolina Hermida-Merino, Martín Pérez-Rodríguez, Manuel M. Piñeiro, and María José Pastoriza-Gallego*

Received Xth XXXXXXXXXXXX 20XX, Accepted Xth XXXXXXXXXXXX 20XX

First published on the web Xth XXXXXXXXXXXX 200X

DOI: 10.1039/b000000x

The rheological behavior of ethylene glycol-based nanofluids containing exfoliated graphite nanoplatelets has been carried out using a cone-plate Physica MCR rheometer. Initial experiments based on flow curves were carried out, the flow curves were based on the controlled shear stress model, these tests show that the studied nanofluids present non-Newtonian shear thinning behavior with yield stress. Furthermore, linear viscoelastic experiments were conducted in order to determine the viscoelastic behavior: using strain sweep and frequency sweep tests the storage and loss modulus were determined. The fractal dimension (D_f) was estimated from the suspension static yield-stress and volume fraction (ϕ) dependence, and was determined to be $D_f=2.36$, a value consistent with a process of aggregation of RLCA type (reaction limited cluster aggregation). This value is unusual if compared with other nanofluids, and can be regarded as a results of the bidimensionality of the suspended nanoplatelets. Finally, creep-recovery tests and mechanical models confirm the viscoplastic nature of our nanofluids, a feature never shown so far for this type of systems, increasing the solid-like character in the range of concentrations studied if compared with other nanofluids reported in literature. This is a result of the combination of a remarkable internal structure and strong interactions, which evidence an unexpected behaviour sharing many solid-like features

1 Introduction

Graphene, a single-atom-thick sheet of hexagonally arranged sp^2 -bonded carbon atoms, has attracted much attention since it was experimentally isolated by Novoselov *et al.*¹. The two-dimensional (2D) material exhibits exceptionally high crystal and electronic quality, and it has already revealed a plethora of amazing physical properties and potential applications². This includes high values of Young's modulus, fracture strength, mobility of charge carriers, and specific surface area, plus fascinating transport phenomena such as the quantum Hall effect³. Recent research reveals that the in-plane thermal conductivity of a suspended single-layer graphene is as high as 5200 W/mK⁴. Because singlelayer graphene sheets are finite and dimensional limitations influence the electronic properties of graphene, graphene-based materials can be categorized according to the dimensions of sheets in the parallel and perpendicular directions of the layers. Among them, exfoliated graphite nanoplatelets (xGnP) (10-100 graphene layers, 3-30 nm thick), which combine the layered structure and low price of nanoclays with the superior mechanical, electrical and thermal properties of carbon nanotubes, are very cost effective and can simultaneously provide a multitude of physical and chemical property enhancements⁵. The properties of xGnP are independent of the number of layers and show similar electro-

chemical behavior to graphene⁶. Although the number of articles on xGnP has increased^{7,8}, data on their thermodynamic properties, thermophysical description, and molecular modeling properties are relatively scarce. Nanofluids, which are suspensions of nanoparticles in fluids⁹, have promising potential applications in microelectronics, energy supply and transportation because of their intriguing properties such as the increased thermal conductivity in certain cases, long-term stability, and prevention of clogging in microchannels¹⁰. The nanoscale size range of the suspended particles produces unexpected behaviour in some cases for thermophysical and transport properties. In fact it was the initial report of unusual thermal conductivity enhancements what boosted research on nanofluid characterization. After a certain rush period, these enhancements were demonstrated not to be so general nor so high¹¹. Nevertheless, the discussion about which are the heat and mass transfer mechanisms for this type of systems represents an open and active debate, and some nanofluids do exhibit unexpected non classical thermophysical and elastic properties¹².

Recently, a significant number of studies have been conducted on the use of carbon-based nanostructures like carbon nanotubes¹³, single-wall carbon nanotubes¹⁴, multi-wall carbon nanotubes¹⁵, graphite¹⁶, graphene oxide¹⁷, and graphene¹⁸ to prepare nanofluids. Most of these investigations are devoted to the measurement of thermal behavior. All such applications require motion of nanomaterial within the fluid,

Departamento de Física Aplicada, Universidade de Vigo, Spain.

*Corresponding author e-mail: mjgg@uvigo.es

or displacement of the bulk suspension itself. Thus, the innate need to understand the rheological behavior of carbon-based suspensions is of primary importance for development of the aforementioned technologies.

Shear viscosity of nanofluids obtained from originally Newtonian base fluids may exhibit either Newtonian^{19–21} or shear-thinning^{22?–29} behavior depending on several factors. Some of them are material, size, shape and nanoparticle concentration, and also type of base fluid. Structured fluids as colloidal gels, microgel suspensions, dense suspensions, concentrated emulsions and foams are yield stress fluids. The yield stress of a material is defined as the minimum shear stress that must be overcome to make a material flow. The existence of a yield stress has been debated in the literature^{30–33} on the grounds that any material will flow given long enough time. Yield stress or viscoplastic materials have a complex microstructure. Emady *et al.*³⁴ have recently suggested that most yield stress materials are based on either colloidal glasses or colloidal gels. As a consequence of this structural complexity, the characterization of these materials has been historically rather challenging^{35,36}. Several techniques can be used to determine yield stress³⁷. In this study, exfoliated graphite nanoplatelets (xGnP) were dispersed in pure ethylene glycol (EG) in various volumetric concentrations, an stabilized by high-power ultrasonication. Stabilization mechanisms are analyzed by UV-visible spectrophotometry, and the rheological behavior of the suspensions was determined via non-linear and linear viscoelastic measurements, yielding as we will demonstrate a profile of highly structured soft matter, with even typical features of solid-like behaviour.

2 Experimental

2.1 Materials

Commercial exfoliated graphite nanoplatelets grade C were supplied by XG Sciences, Inc. This material consists of several layers of exfoliated graphite with average surface area of approximately $750 \text{ mm}^2 \text{ g}^{-1}$ and nominal flake thickness of 1–5 nm. Ethylene glycol was supplied by Aldrich (99 %).

2.2 Characterization

X-Ray photo-electron spectroscopy measurements were carried out in a Thermo Scientific K-Alpha ESCA instrument equipped with aluminium $\text{K}\alpha_1$, 2 monochromatized Al $\text{K}\alpha$ radiation at 1486.6 eV X-ray source. The base pressure in the chamber was maintained at about $3 \cdot 10^{-9}$ mbar. Photoelectrons were collected from an angle of 90° relative to the sample surface. A constant analyzer energy mode (CAE) was used with a pass energy of 100 eV and 20 eV for the survey spectra and high resolution spectra, respectively. Binding energies

were calibrated using the C 1s peak at 285.0 eV as internal standard.

The morphology of xGnP were examined by high resolution scanning electron microscopy (FEG-SEM) using a JEOL JSM-6700-F. FGE- SEM samples were prepared by deposition of the nanopowder on top of a carbon substrate.

2.3 Sample preparation and stability

Homogeneous and stable suspensions of xGnP in Ethylene glycol (EG) were studied. The nanoparticle powder was weighted using a Mettler AE-240 electronic balance, whose accuracy is $5 \cdot 10^{-5}$ g. The powder was dispersed into a predetermined volume of the base fluid to obtain the desired weight fraction up to 20 wt%. Particles were dispersed by ultrasonic treatment with an Ultrasonic Bath (Clifton, 80W). Ultrasound is very effective in the destruction of aggregates by using the collapse of the unstable cavitation bubbles that grow in the ultrasonic field. The implosive collapse of the bubbles rips the platelets apart and restricts the aggregation of the exfoliated graphite sheets, leading to a stable dispersion of these in the matrix. The stability of the nanofluid was evaluated using a spectrometer Agilent HP 8453 UV-Vis equipped with a thermostated cell carrier, at different times of sonication.

2.4 Rheological measurements

Rheological analyses were performed with a Physica MCR 101 Rheometer (Anton Paar, Graz, Austria), using a cone-plate geometry (CP 25-1). The equipment allows to control torques between $0.5 \mu\text{N}\cdot\text{m}$ and $125 \text{ mN}\cdot\text{m}$ and normal force from 0.1 to 30 N. All experiments are conducted at a constant gap of 0.048 mm, and an initial stabilization period of 100 s is given for achieving constant temperature (303.15 K) using a Peltier system. Different types of experiments were carried out to investigate the nanofluid rheological behavior. The first one is a non-linear viscoelastic experiments, usually referred to as flow curves, in which shear viscosity variation with shear rate is measured. These experiments were performed at shear rates up to 10000 s^{-1} , at different weight fractions up to 20 wt%. The linear viscoelastic measurements constitute the second group of the experiments. In these measurements first linear viscoelastic (LVE) region was determined by measuring store (G') and loss (G'') moduli of the nanofluids in the strain range between 0.01 % to 1000 % at a constant angular frequency of $10 \text{ rad}\cdot\text{s}^{-1}$, at different weight fractions up to 20 wt% and 303.15 K. Frequency sweep measurements were carried out in the frequency range of 0.1 to $600 \text{ rad}\cdot\text{s}^{-1}$ by applying a strain of 0.1 %, at different weight fractions up to 20 wt% and 303.15 K. Furthermore transient deformation in the nanofluids was evaluated by creep and recovery measurements. Different shear stress loads inside the linear viscoelas-

tic region were applied for 300 s. Creep measurements were recorded following another 600 s of recovery period. Three replicates at each experimental condition were carried out.

3 Results and discussion

3.1 Characterization of exfoliated graphite nanoplatelets

The elemental chemical composition of the surface of xGnP was confirmed using X-Ray photoelectron spectroscopy. Figure 1-Left shows the survey spectra of xGnP. In this figure we can observe a strong peak at around 285 eV, attributed to the elemental sp^2 and sp^3 carbon atoms of the exfoliated graphite nanoplatelets (C 1s) and a peak at approximately 532 eV, ascribed to the oxygen atoms (O 1s). Quantitative peak analysis revealed that the carbon concentration is 93.94 % at. and the oxygen concentration is 5.95 % at., with an amount of 0.11 % at. of nitrogen. Morphology of xGnP was examined by high resolution scanning electron microscopy (FEG-SEM). Typical FEG-SEM images of xGnP nanopowder are presented in Figure 1-Right, evidencing that the nanoplatelets are crumpled and folded. The occurrence of crumpling and scrolling is intrinsic to exfoliated graphite nanoplatelets and is caused by the bidimensional structure becoming thermodynamically stable via bending. The nanometric platelets tend to agglomerate into micron-size domains, as observed in this figure.

3.2 Stability

The stability of the nanofluid was evaluated using a UV-Vis spectrometer at different sonication times. Figure 2-Left shows a typical recording for the optical absorption spectrum of EG/xGnP nanofluid (0.001 wt%). The wavelength value was fixed at $\lambda=266$ nm, and the absorbance time evolution for the samples at different sonication times was analyzed, Figure 2-Right. The graph shows that the best stability is obtained applying 1.5 hours of sonication, the absorbance decrease in 24 h was found to be only 4.2 %. With the aim to verify if this decrease is representative of the real concentration, we have developed a second procedure to estimate the stability of nanofluids. In this case, a freshly 20 wt% nanofluid (20 mL) was prepared applying 1.5 hours of sonication with the ultrasonic bath, and then this nanofluid was transferred to a water-jacketed cell at 303.15 K. Aliquots (5 μ l) of the nanofluid are removed at specific time intervals (three aliquots each time) and added immediately to three flasks containing 20 mL of Ethylene Glycol. These resultant solutions were dispersed applying 15 min of sonication with the ultrasonic bath. We evaluated the stability of this nanofluid by measuring the absorbance at 266nm of each solution at different times. Figure 3 evidences the percent decrease of the absorbance registered using both procedures at different con-

centrations, showing that this departure function rises slightly with time, the absorbance decrease in 10 h was found to be 4 % for 20 wt% EG/xGnP nanofluid and 2.8% for 0.001 wt%, so the absorbance decrease in this case is nearly independent of the concentration of nanofluids. These results indicate that the sample at 20 wt% is stable and adequate for the type of measurements performed in this work, where the time from sample dispersion to the experimental measurements was very short.

3.3 Non-linear viscoelastic measurements

Figure 4 shows the shear viscosity (μ) as a function of shear rate ($\dot{\gamma}$), usually referred to as flow curves, of EG and six different weight fraction of EG/xGnP nanofluids (1, 2.5, 5, 10, 15 and 20 wt%). The base fluid viscosity is independent of $\dot{\gamma}$ indicating Newtonian behavior for EG. On the other hand, EG/xGnP nanofluids show shear-thinning with yield stress, which represents a non-Newtonian behavior, as we can observe a decrease of shear viscosity with the applied shear rate. As concentration rises a Newtonian plateau appears in the lowest shear rate region, and the shear thinning property is more pronounced due to the stronger sheet-sheet and multi-sheet interactions with the increase in concentrations. Shear-thinning of well-dispersed suspensions can be linked to the modifications in the structure and arrangement of interacting particles³⁸. Shearing may cause the particles to orient in the direction of flow and its gradient. This can break agglomerates and hence reduce the amount of solvent immobilized by the particles. The interaction forces may then decrease and cause a lowering in the flow resistance and the apparent viscosity of the system. An important class of non-Newtonian materials exhibits the so-called yield stress, absorbing in a first stage the stress energy without flowing, until the yield stress threshold is exceeded and significant deformation occurs. This observed behaviour can be associated to a certain extent to the mild re-orientation of exfoliated graphite nanosheets at high shear rate. The orientation anisotropy may produce a liquid crystal-like structure which can form a stable nematic liquid crystal in Ethylene Glycol. This behavior has been reported previously for suspensions of exfoliated graphite oxide nanosheets, that can behave like colloids in water thus avoiding agglomeration or re-stacking³⁹. Therefore, and following this short range partially ordered spacial arrangement these materials behave as solids when the local shear is below the yield stress.

Once the yield stress is exceeded, the material flows with a non-linear stress-strain relationship, either as a shear-thickening fluid, or a shear-thinning one. Some examples of fluids behaving in this manner include paints, food products, plastics, slurries, pharmaceutical products, polymeric solutions, paper pulp⁴⁰ and semisolid materials⁴¹. To model the stress-deformation behavior, several constitutive relations

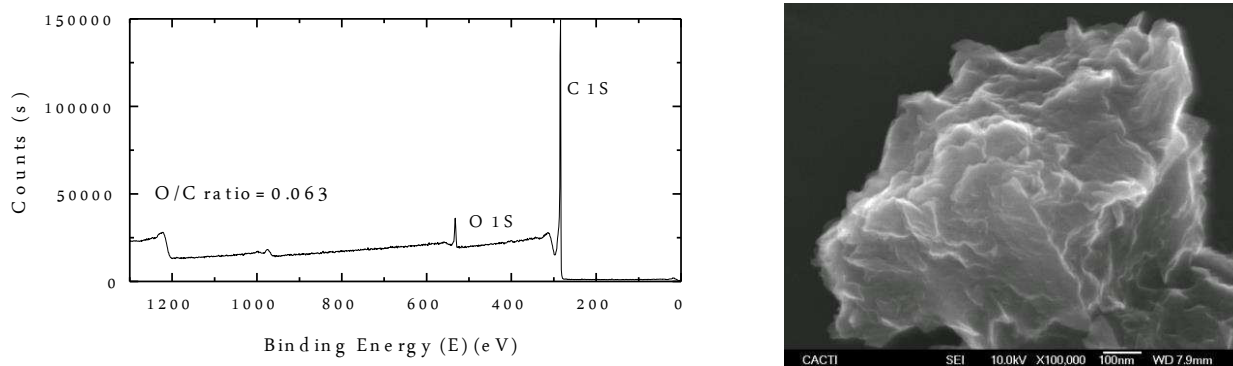


Fig. 1 Survey spectra (left) and FEG-SEM, 100000 \times , JEOL JSM-6700F (right) of dry commercial xGnP nanopowder.

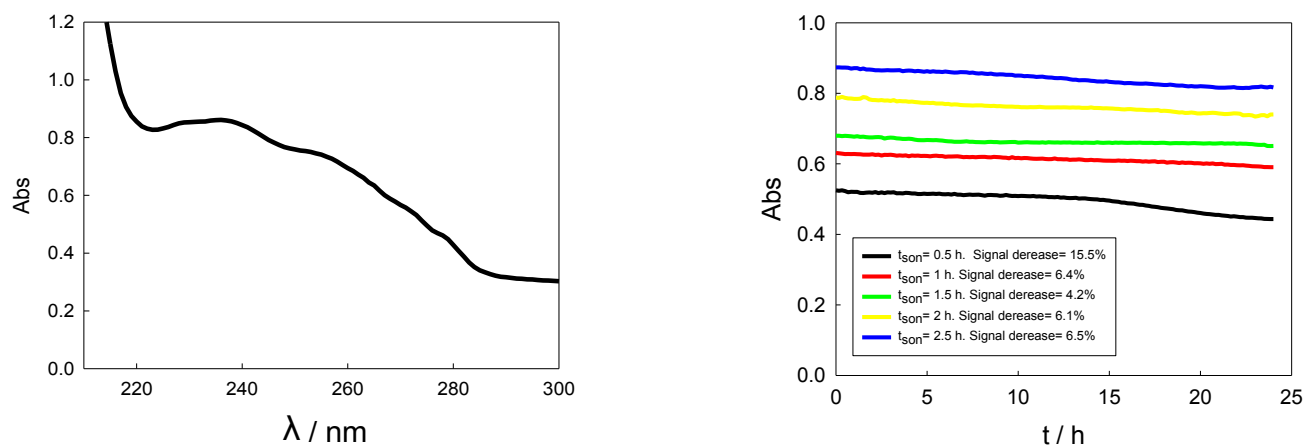


Fig. 2 UV-Vis absorption spectrum (left) of EG/xGnP nanofluid, 0.001 wt%, $T = 303.15$ K, and influence of the time of sonication in the kinetic deposition of EG/xGnP nanofluids (right), $\lambda = 266$ nm, $T = 303.15$ K

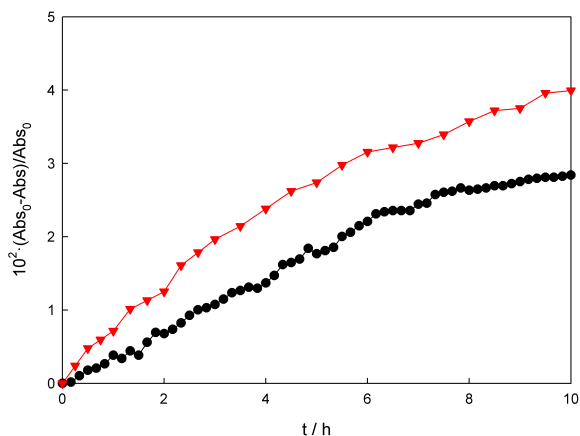


Fig. 3 Percent decrease of the absorbance, $10^2(\text{Abs}_0 - \text{Abs})/\text{Abs}_0$ with time of EG/xGnP nanofluids, circle, 0.001 wt% (First procedure, 1.5h sonication time); inverted triangle, 20 wt% (Second procedure), $\lambda = 266$ nm, $T = 303.15$ K

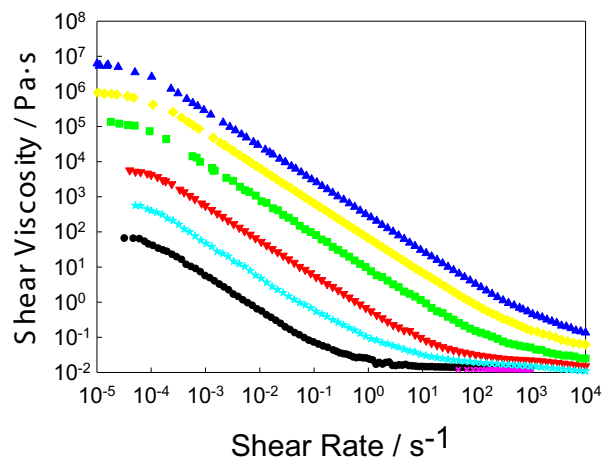


Fig. 4 Shear viscosity vs. shear rate ($\dot{\gamma}$) dependence of EG/xGnP nanofluids. At 303.15 K for different weight fractions: pink multiplication sign, EG; circle, 1 wt%; star, 2.5 wt%; inverted triangle, 5 wt%; square, 10 wt%; diamond, 15 wt% and triangle, 20 wt%.

have been proposed and different yield criteria have been used. Two of the most useful⁴² and popular models have been the Bingham model, which is a modification of the Newtonian model to incorporate a yield stress and the Herschel-Bulkley model, which is the equivalent modification of the power-law model⁴³. In simple shear flow these models take the form: Bingham model:

$$\sigma = \sigma_y + \mu \dot{\gamma} \quad \text{For } |\sigma| > \sigma_y \quad \dot{\gamma} = 0 \quad \text{For } |\sigma| \leq \sigma_y \quad (1)$$

Herschel-Bulkley model:

$$\sigma = \sigma_y + K \dot{\gamma}^p \quad \text{For } |\sigma| > \sigma_y \quad \dot{\gamma} = 0 \quad \text{For } |\sigma| \leq \sigma_y \quad (2)$$

Where σ is the shear stress, $\dot{\gamma}$ is the shear rate, σ_y is the dynamic yield stress, μ is the Newtonian viscosity, K is the consistency index and p is the power-law index. Note that when the shear stress is below the yield stress a solid structure is formed (unyielded). Also, when the power-law index equals unity and the consistency index is equivalent to the viscosity, the Herschel-Bulkley model reduces to the Bingham model. Both models are viscoplastic but inelastic, i. e. they cannot account for viscoelastic phenomena such as stress relaxation and normal stresses exhibited in shear flows. Papanastasiou⁴⁴ proposed a novel constitutive equation for materials with yield, where a material parameter controls the exponential growth of stress and which is valid for both yielded and unyielded areas. In simple shear flow, Papanastasiou's modification to the Herschel-Bulkley model gives:

$$\sigma = \sigma_y [1 - e^{-m\dot{\gamma}}] + K \dot{\gamma}^p \quad (3)$$

Where m is a regularization parameter (with units of time), which controls the exponential growth of stress. Figure 5 shows the experimental values of shear stress vs. shear rate of EG/xGnP nanofluids (1, 2.5, 5, 10, 15 and 20 wt%) and their fit with the Papanastasiou's modification to the Herschel-Bulkley model (equation 3) with $m > 10000$ s. The flow parameters of this fit are shown in Table 1. Good adjustments are obtained for all samples, reaching shear stress average deviations around 3%. The n values range from 0.988 to 0.748 decreasing exponentially when the weight fraction increases, which evidences that the shear thinning behavior is more noticeable as nanoparticle concentration increase⁴⁵. Dynamic yield stress and consistency index values increase nearly exponentially with weight fraction.

3.4 Linear viscoelastic measurements

The following step was to perform oscillatory or dynamic experiments to determine viscoelastic behaviour. First, strain sweep test at constant $\omega = 10$ rad·s⁻¹ were carried out to identify the linear viscoelastic region in the strain range from

Table 1 Yield stress (σ_y), Consistency index (K), the stress growth exponent (m) and Power-law index (p) parameters for EG/xGnP nanofluids at 303.15 K and different weight fractions.

Weight Fraction wt%	Yield Stress σ_y (Pa)	Consistency Index K (Pa·s ^p)	Power-law p
1	0.0058±0.0005	0.0141±0.0001	0.988±0.001
2.5	0.065±0.005	0.0244±0.0001	0.915±0.002
5	0.541±0.001	0.0446±0.0001	0.884±0.003
10	8.7±0.2	0.171±0.009	0.786±0.006
15	65.1±0.4	0.550±0.002	0.747±0.004
20	279±1	1.4±0.1	0.719±0.008

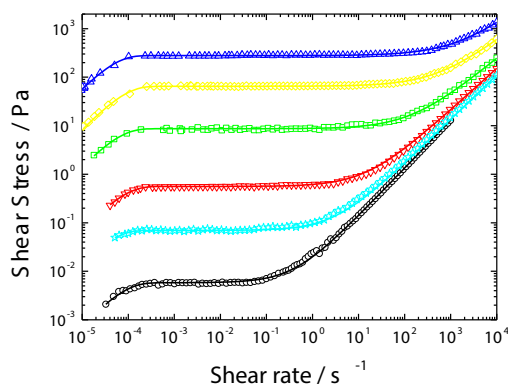


Fig. 5 Shear stress vs. shear rate ($\dot{\gamma}$) dependence of EG/xGnP nanofluids. At 303.15 K for different weight fractions: circle, 1 wt%; star, 2.5 wt%; inverted triangle, 5 wt%; square, 10 wt%; diamond, 15 wt% and triangle, 20 wt%. The solid lines represent the fit using the Papanastasiou's modification to the Herschel-Bulkley model

0.01 to 1000 %. As shown in Figure 6, both storage (G') and loss (G'') moduli increase with weight fraction. The linear regime where G' is constant regardless of strain amplitude is clearly observed, and then the value decreases for all weight fractions. On the other hand, G'' goes through a maximum, exhibiting a so-called overshoot phenomenon. The interpretation of this phenomenon is that when an external strain is imposed, the structure resists up to a certain strain, while G'' increases, and then the internal structure is lost by the disaggregation of nanoparticles, due to large deformations over the critical strain after which the nanoparticles align with the flow field, decreasing both G' and G'' . In order to evidence the well-defined linear viscoelastic range of this test, typical stress-strain curves are also displayed in Figure 7 for all weight fractions. Table 2 lists static yield stress and critical strain values. Static yield stress and critical strain values increase linearly (in logarithmic scale) with volume fraction. In the bulk of a flocculated suspension, particles will adhere to each other building up a porous network. This network is stabilized mainly by means of van der Waals interactions between particle surfaces^{46,47}. The self-similar structure of the network and aggregate geometry can be described using fractal analysis, as was shown by Shih *et al.*⁴⁸, being suspension yield stress (Y) related with the volume fraction (ϕ) through:

$$Y = \alpha \phi^n \quad (4)$$

where α is a constant related with the inter-particle separation and the zeta potential. The exponent n can be evaluated from the suspension Y - ϕ relationship and is further related to the fractal dimension (D_f) of the flocculated network by the equation:

$$n = (d + X)/(d - D_f) \quad (5)$$

where d and X stand for the Euclidean dimension of the whole system and the aggregate backbone (or aggregate main structural element), respectively⁴⁸. Fitting the experimental data of Table 2 to the equation 4, the value obtained for n is 7.78 ± 0.38 and $\alpha = (3.78 \pm 1.14) \cdot (10)^5$ with a Pearson correlation coefficient $r^2 = 0.994$ (see Figure 8). We may calculate the fractal dimension (D_f) from the slope n by assuming the fractal

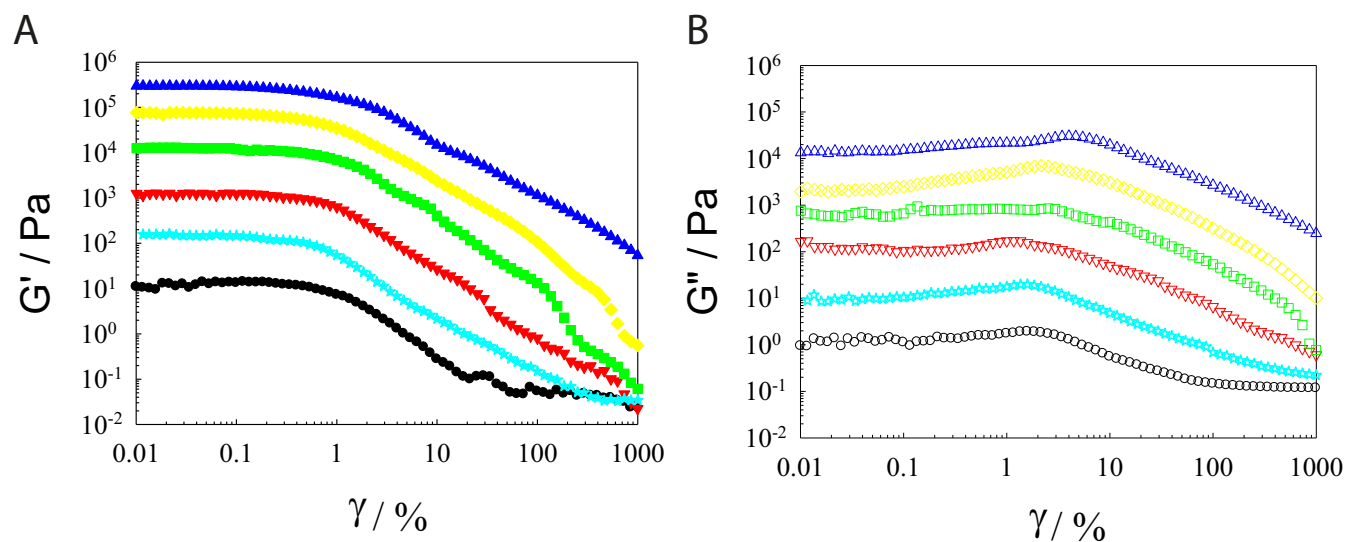


Fig. 6 Storage (G') (A) and loss (G'') (B) moduli vs. strain (γ) dependence at $10 \text{ rad}\cdot\text{s}^{-1}$ and 303.15K of EG/xGnP nanofluids for different weight fractions: circle, 1 wt%; star, 2.5 wt%; inverted triangle, 5 wt%; square, 10 wt%; diamond, 15 wt% and triangle, 20 wt%.

Table 2 Static yield stress (Y) and critical strain (γ_c) values for different EG/xGnP nanofluids at 303.15K and $\omega=10 \text{ rad}\cdot\text{s}^{-1}$

Weight Fraction (wt%)	Volume Fraction ϕ (v/v)	Static Yield Stress Y (Pa)	Critical Strain γ_c (%)
1	0.0360	0.0252	0.185
2.5	0.0865	0.264	0.215
5	0.1627	2.80	0.251
10	0.2909	36.2	0.341
15	0.3945	250.0	0.465
20	0.4800	1260	0.632

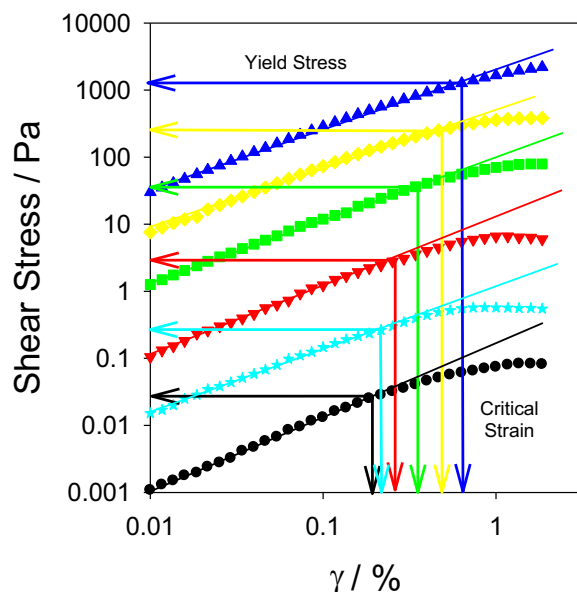


Fig. 7 Store (G') (A) and loss (G'') (B) moduli vs. strain (γ) dependence at $10 \text{ rad}\cdot\text{s}^{-1}$ and 303.15K of EG/xGnP nano-fluids for different weight fractions: circle, 1 wt%; star, 2.5 wt%; inverted triangle, 5 wt%; square, 10 wt%; diamond, 15 wt% and triangle, 20 wt%.

dimension of the backbone of the clusters X equals unity⁴⁹ and Euclidean dimension is $d = 3$, the fractal dimension for EG/xGnP nanofluids is $D_f^{(1)} = 2.49$. If we consider alternative values for the backbone dimension, namely $X = 2$ and $X = 3$, the fractal dimension results in $D_f^{(2)} = 2.36$ and $D_f^{(3)} = 2.23$ respectively. All calculated values of D_f are close to 2.3, the characteristic value of the aggregation type called *reaction limited cluster aggregation* (RLCA), and considerably far from 1.8, the reference value for a *diffusion limited cluster aggregation* (DLCA) process⁵⁰. This result is independent of the backbone dimension considered, and strongly suggests that the aggregation present is of the RLCA type, building compact structures with effective dimension greater than 2. Moreover, the high value obtained for n is also characteristic of this aggregation scheme. Backbone dimension is usually considered to be equal to unity, due to the abundance of systems with chain-like or dendritic aggregates. In our case, that value would yield a very high fractal dimension, 2.49, close to a pure liquid dimension, $D_f(l) = 2.55$ ⁵¹, and considerably greater than other strong-interacting colloidal aggregates, as in magnetite suspensions ($D_f(\text{mag}) = 2.27$), where magnetic dipolar interactions determine the aggregation process²⁷. The fractal dimension of a liquid is a consequence of the effective breaking of some bonds when compared with the corresponding

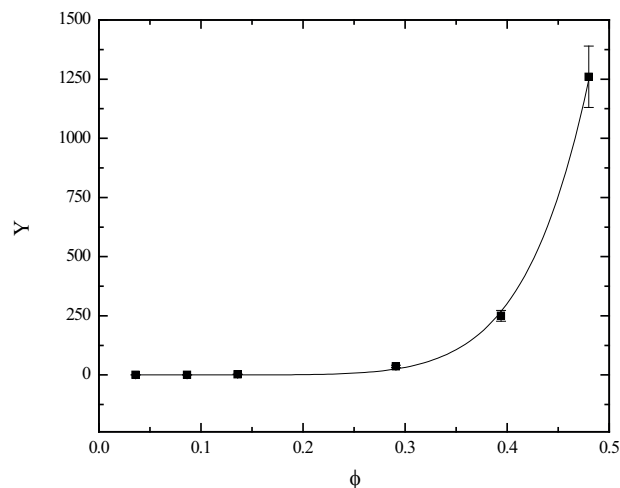


Fig. 8 Static Yield stress (Y) as a function of volume fraction (ϕ). Experimental data, squares with error bars, were fitted to equation (4), obtaining the solid line for parameter $n = 7.78 \pm 0.38$.

solid, so it can be regarded as a limit for the bonding dimension of pure substances. Therefore, it would be unrealistically high for a substance in a mixture, as the case of a colloidal suspension. Considering the exfoliated graphite nanoparticles morphology, that consist of superimposed sheets of real exfoliated graphite, it can be supposed that the aggregates will grow preferentially following the planes of the sheets, and so the backbone dimension should be close to 2. The analysis presented of SEM images supports this hypothesis for micron size aggregates. For $X = 2$, we obtained $D_f^{(2)} = 2.36$, as shown above, very close to the characteristic value of a RLCA type process. Moreover, the nanoparticles can be deformed, making complex structures as planar tees or loops when aggregate, building bi-dimensional and also three-dimensional backbones, and laying the backbone dimension in some point between 2 and 3. Therefore, it seems reasonable to obtain a D_f value greater than the theoretical one when considering $X = 2$ and lower when considering $X = 3$. In figure 9, D_f is represented as a function of X , being lower for increasing X . This is to say, if we consider $X' > 2$, then $D_f(X') < D_f^{(2)}$, and inversely, if $X' < 3$, then $D_f(X') > D_f^{(3)}$, confirming that backbone dimensions between 2 and 3 are compatible with RLCA aggregation type in xGnP nanoparticles. The conclusion is then that the aggregation follows a RLCA scheme, and the whole dimension of the aggregates backbone is $X = 2$. Then frequency sweep tests were carried out in the linear viscoelastic region, with angular frequencies ranging for 0.1 to $600 \text{ rad}\cdot\text{s}^{-1}$ and a constant strain value of 0.1 %. The experimental data of storage and loss moduli are shown in Figure 10. For these nanofluids the storage modulus exceeds the loss modulus, $G' > G''$ for the whole angular frequency range stud-

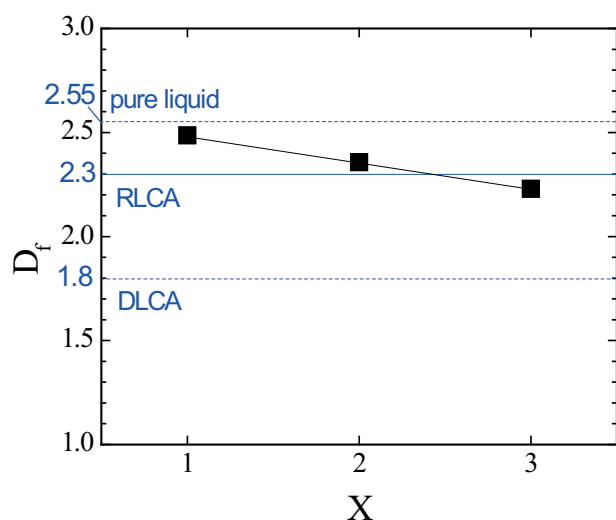


Fig. 9 Fractal dimension of aggregates (D_f) depending on backbone dimension (X) calculated using equation (5). Some characteristic values of D_f (pure liquid, RLCA and DLCA) are shown in blue for reference.

ied. G' and G'' are practically constant in this angular frequency range, typical of "solid-like" complex fluids, and both increase with volume fraction. The experimental data for the equilibrium modulus of exfoliated graphite nanofluids at low frequencies were modeled as a function of concentration according to a percolation expression as follows⁵²:

$$\log(G') = A + B \log(\phi - \phi_0). \quad (6)$$

where A and B are constants and ϕ_0 is ϕ at the threshold, and the equation can be applied only near the percolation threshold. The experimental data measured at a low frequency (10 rad/s) were fitted to Equation 6, leaving as adjustable parameters the concentration at the threshold (ϕ_0) and the parameters A and B . As shown in Figure 11, the experimental data are well modeled by the Equation 6, from which a close to zero critical concentration is determined. Therefore, our experiments have been performed at concentrations that are well beyond the percolation threshold, and can be easily classified as gels. For these exfoliated graphite nanofluids, the van der Waals interactions are so strong that give rise to large structures even at very low concentrations.

Finally creep and recovery profiles of these nanofluids were obtained. Creep testing entails applying a small constant stress to a sample and monitoring its deformation over time. When a viscoelastic material is subjected to a creep test the initial stage of the test is dominated by elastic, recoverable deformation. As the test progresses the sample reaches an elastic equilibrium and only residual viscous non-recoverable flow persists. From the gradient of the strain/time plot in the later

Table 3 Constant stress (σ_0), zero-shear viscosity (μ_0), equilibrium elastic strain (γ_{eq}) and equilibrium recoverable compliance (J_e^0) values for different EG/xGnP volume fraction ϕ at 303.15 K

ϕ (v/v)	σ_0 (Pa)	μ_0 (Pa·s)	γ_{eq} (%)	J_e^0 (Pa ⁻¹)
0.1627	0.008	5459	0.2150	0.11125
0.2909	0.5	204496	0.1984	0.00226
0.3945	4	991375	0.3059	0.000295
0.4800	50	7073236	0.4495	0.0000516

viscous-flow stage of the test the value of zero-shear viscosity (μ_0) can be calculated. By extrapolating the straight-line regression from this part of the curve to an intercept on the strain axis it is possible to obtain the equilibrium elastic strain (γ_{eq}), representing the maximum elastic recoverable strain under the specific imposed stress. Then, for a creep experiment, a constant stress (σ_0) inside the linear viscoelastic region is applied at time zero to the relaxed samples during a time that may be considered asymptotically infinite (300 s. in this case), and the sample strain trend is recorded. At 300 s, the stress is removed and strain variation is again recorded. We have selected the recovery time to be twice the creep time. A representative example of this creep and recovery profile is represented in Figure 12, for 20 wt% exfoliated graphite/EG nanofluid at a constant stress of 50 Pa. The zero-shear viscosity and the equilibrium elastic strain calculated in the later viscous-flow stage for all nanofluids are shown in Table 3. The constant stress (σ_0) that should be applied for 1 wt% and 2.5 wt% nanofluids to ensure that the samples were inside the linear viscoelastic region were too low for performing the creep-recovery test with reasonable accuracy, so these two low concentration samples were not considered. Strain values can be divided by the applied stresses to obtain compliance, denoted as $J(t)$:

$$J(t) = \gamma(t)/\sigma_0. \quad (7)$$

a magnitude useful for cases when different stresses are employed and the results are to be compared, this enables the direct visual overlapping of the results obtained. In the linear viscoelastic region $J(t)$ will be independent of the applied stress (Figure 13-left). The recovery profile of our nanofluids are represented in Figure 13-right together with the recoverable compliance $J_r(t)$, defined as,

$$J_r(t) = (\gamma_u - \gamma_r(t))/\sigma_0. \quad (8)$$

Being σ_0 the constant imposed stress, $\gamma(t)$ the strain values at different times, γ_u the initial deformation at $t_2 = 300$ s, in the recovery test, and $\gamma_r(t)$ the recoverable strain values at different times. The equilibrium recoverable compliance J_e^0 is a very sensitive measurement of the elasticity, defined as,

$$J_e^0 = (\gamma_u - \gamma_e)/\sigma_0. \quad (9)$$

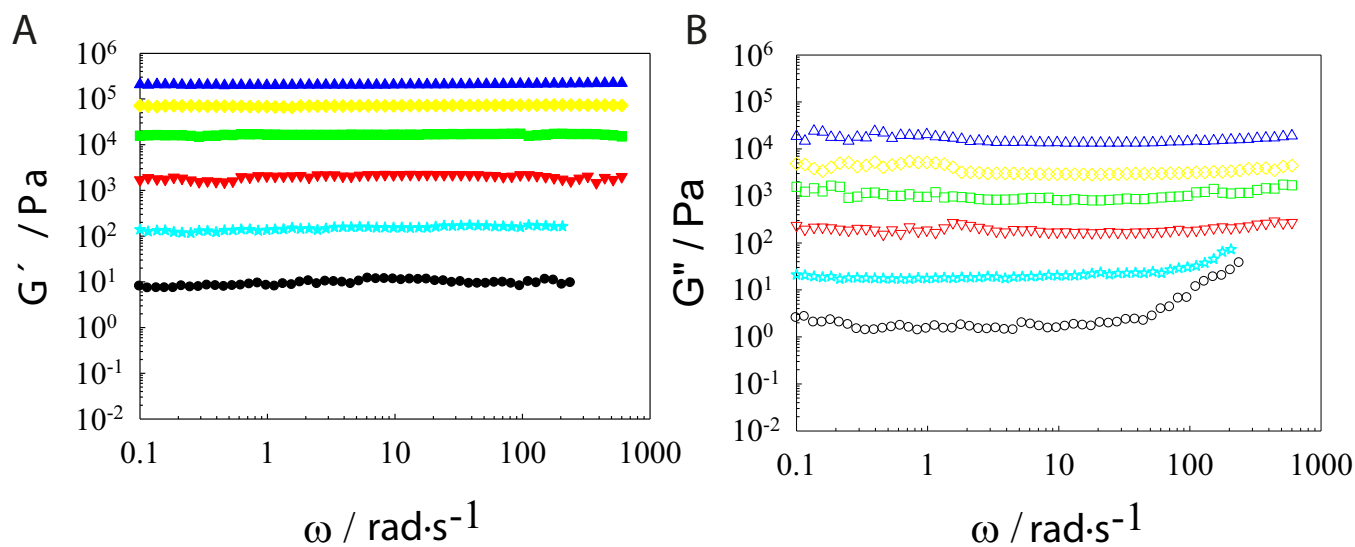


Fig. 10 Storage (G') (A) and loss (G'') (B) moduli vs. angular frequency (ω) dependence at a constant strain (0.1 %) and 303.15K of EG/xGnP nanofluids for different weight fractions: circle, 1 wt%; star, 2.5 wt%; inverted triangle, 5 wt%; square, 10 wt%; diamond, 15 wt% and triangle, 20 wt%.

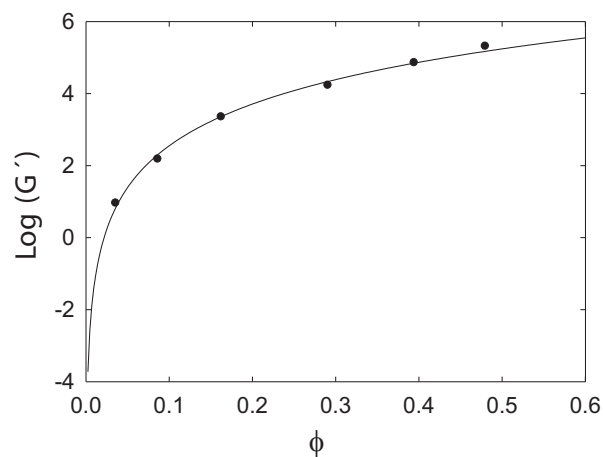


Fig. 11 Logarithmic storage modulus, $\text{log}(G')$, vs. volume fraction, fitted using the percolation model (equation 6) at 10 rad·s $^{-1}$ and 303.15 K with 0.1 % of strain

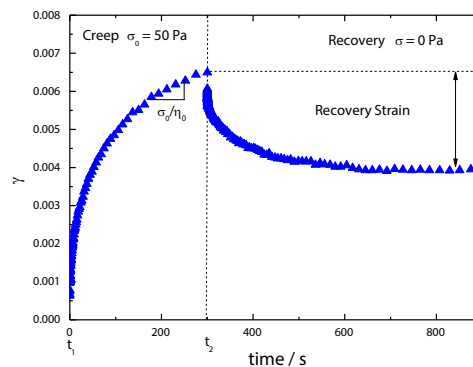


Fig. 12 Creep and recovery curve for 20 wt% of EG/xGnP nanofluids at applied stress of 50 Pa

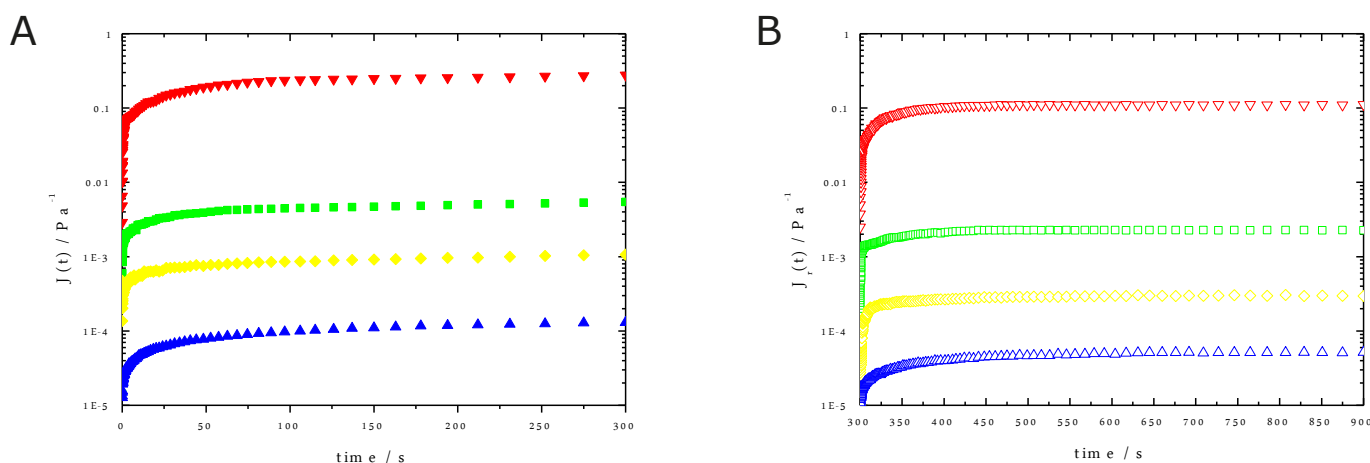


Fig. 13 Compliance curves (A) and recoverable compliance curves (B) of EG/xGnP nanofluids, at 303.15K for different weight fractions: inverted triangle, 5 wt% ($\sigma_0=0.008$ Pa); square, 10 wt% ($\sigma_0=0.5$ Pa); diamond, 15 wt% ($\sigma_0=4$ Pa) and triangle, 20 wt% ($\sigma_0=50$ Pa)

where γ_u the initial deformation at $t_2=300$ s, and γ_e the final deformation at $t=900$ s (in the equilibrium zone). The values obtained are show in Table 3.

3.4.1 Mechanical Model for description of the rheological Data.

In order to set an adequate mechanical model for the studied system, both elastic and viscous properties must be taken into account, as deduced from the results in the precedent paragraphs, and from direct inspection of the EG/xGnP samples. Therefore, the first option can be the Burgers model, which is composed of Maxwell and Kelvin-Voight elements, connected sequentially⁵³⁻⁵⁵. A scheme of the mechanical elements and the models used in this work is shown in Figure 14. Maxwell element describes the viscoelastic liquid-like behavior, by means of one ideal spring and one hydraulic damper filled with an ideal Newtonian liquid, arranged in a serial disposition. Kelvin-Voight element is the equivalent for solid-like behavior, and is composed of the same elements (spring and damper) except that they are arranged in parallel in this case. For a creep-recovery experiment, the Maxwell model predicts an immediate initial jump in the compliance, $J(t)$, followed by a linear increase, during the creep period, and an instantaneous decrease after stress removal, without gradual relaxation. However, in our experiments, we observe a non-linear increase of $J(t)$ during the creep period and also a significant slow relaxation after removal of the applied stress, two features that evidence that exfoliated graphite nanofluids do not behave as a simple Maxwell body upon shear. According to the Kelvin-Voight model, the deformation should attain a constant value (plateau) after a certain creep time. In the recovery regime, no instantaneous decrease in $J(t)$ or residual deformation is expected, whereas we observe both features in our experiments. This comparison shows that exfoliated

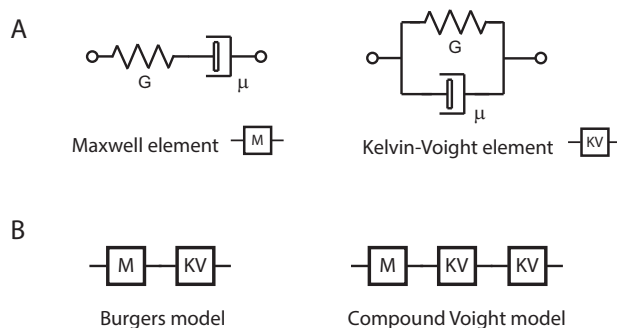


Fig. 14 A: Simple elements in mechanical models for viscoelasticity, spring ideally models the elasticity and damper the viscosity. B: Burgers and compound Voight models as a combination of simple elements.

graphite nanofluids can not be described either with a Kelvin-Voight model only. Therefore, a simple ideal model solely, as Maxwell or Kelvin, is not enough to describe the phenomena observed in our experiments and at least a combination of both is necessary, as in the Burgers model. In this model, the compliance during the creep state of the deformation is described by the following equation:

$$J(t) = \frac{t}{\mu_0} + \frac{1}{G_0} + \frac{1}{G_1} \left[1 - \exp\left(-\frac{t}{\lambda_1}\right) \right] \quad (10)$$

where G_0 and μ_0 are the elastic modulus and viscosity in the Maxwell element, G_1 and μ_1 are those in the Kelvin element, and $\lambda_1 = \frac{\mu_1}{G_1}$ is the related characteristic relaxation time of the creep deformation. The compliance during recovery, J_R can be expressed by⁵³:

$$J_R(t) = \frac{t_{CR}}{\mu_0} + \frac{1}{G_1} \left[1 - \exp\left(-\frac{t_{CR}}{\lambda_1}\right) \right] \exp\left(-\frac{t-t_{CR}}{\lambda_1}\right) \quad t > t_{CR} \quad (11)$$

where t_{CR} is the time of creep.

In addition to Burgers model, a compound Voight model was also considered, for better describing the stronger solid-like behavior observed at high concentrations. In this model, an extra Kelvin-Voight element is added to Burgers model, resulting in one Maxwell and two Kelvin-Voight elements connected sequentially. According to this model, the compliance during creep follows the expression:

$$J(t) = \frac{t}{\mu_0} + \frac{1}{G_0} + \frac{1}{G_1} \left[1 - \exp\left(-\frac{t}{\lambda_1}\right) \right] + \frac{1}{G_2} \left[1 - \exp\left(-\frac{t}{\lambda_2}\right) \right] \quad (12)$$

and during recovery, the corresponding one:

$$J(t) = \frac{t_{CR}}{\mu_0} + \frac{1}{G_1} \left[1 - \exp\left(-\frac{t_{CR}}{\lambda_1}\right) \right] \exp\left(-\frac{t-t_{CR}}{\lambda_1}\right) + \frac{1}{G_2} \left[1 - \exp\left(-\frac{t_{CR}}{\lambda_2}\right) \right] \exp\left(-\frac{t-t_{CR}}{\lambda_2}\right) \quad ; \quad t > t_{CR} \quad (13)$$

where G_2 , μ_2 and $\lambda_2 = \mu_2/G_2$ are the elastic modulus, viscosity, and relaxation time of the second Kelvin element, respectively. Compliance data of EG/xGnP nanofluid at different weight fractions were fitted to Burgers model (equations 10 and 11) and compared with the compound Voight model (equations 12 and 13). The results are shown in Figure 15 and parameters are detailed in Table 4.

The fits are in general very good, with Pearson correlation parameter (R^2 adjusted) always above 0.95 and greater than 0.99 in most cases. Pearson coefficient, R^2 values are better for compound Voight than for Burgers in all data sets, so it is tempting to affirm that compound Voight is the better choice in all cases, for both creep and recovery section. Nevertheless, this last affirmation is not necessarily true as compound Voight extends Burgers model with extra adjustable parameters and, consequently, it is expected to fit better the same dataset. Therefore, R^2 solely is not enough to assess the quality and adequacy of the models, and we have to further test their predictive ability with additional magnitudes. Theoretical curves reproduce quite well the experimental results, with the exception of the immediacy of creep time, and for large recovery times also. In these regions, some differences between Burgers and compound Voight models become apparent, specially in the highest concentration (20 wt%) case. If we focus in the creep section of the graphs, we can compare the zero-shear viscosity obtained directly by the mechanical

methods as the μ_0 parameter with the previously calculated values as the slope of the creep curve near the creep time, t_{CR} . The values obtained by the two approaches are in good agreement, with an overall discrepancy below 10 % when using the better fit among the mechanical methods. From this comparison, the quality of the model can be tested, confirming the adequacy of Burgers in 5 wt% case—with only a 6.9 % of difference, while compound Voight reaches the 31.2 % in it—, the equivalence of both models in 10 wt% case—with only a 2.2 % of difference—, and the superior fitting of compound Voight for higher concentrations. Values of G_1 and λ_1 calculated using both models are similar, in creep as well as in recovery sections of the data. Based in the statistical parameters, and coherence of results, we suppose that in the recovery section compound Voight is always more adequate than Burgers method.

4 Conclusions

xGnP/EG nanofluids were rheologically characterized. This work evidences the non-Newtonian nature of EG/xGnP nanofluids, showing shear thinning and dynamic yield stress. All samples show viscoplastic nature, suggesting that a combination of particle aggregation and shape effects is the mechanism for its high-shear rheological behavior. As concentration rises, Newtonian plateaus are found at the lowest shear rate and the flow curves can be described using the Papanastasiou's modification to the Herschel-Bulkley model. Strain sweep tests show that the structural interactions are strong, resulting in large moduli. The fractal dimension of aggregates was calculated, being $D_f = 2.36$. This value is in agreement with a RLCA type aggregation process. Another conclusion from fractal analysis is that the aggregate structure must be laminar, not chain-like, assuming the backbone dimension to be $X = 2$. The frequency sweep tests show that our nanofluids behave as *solid-like* complex fluids. A critical concentration near to zero has been determined, so the interactions are so strong that give rise to large structures even at very low concentrations. The creep-recovery tests confirm the viscoelastic nature of our nanofluids, the zero-shear viscosities have been determined, a critical parameter for applications of these nanofluids as transport fluids, and the melt elasticity has been evaluated. Two mechanical models, Burgers and compound Voight, were tested in order to describe the rheological properties of the nanofluids, the first more oriented towards liquid-like fluids, and the second toward solid-like ones. The fitting of the models confirms that the solid-like character increases with the concentration, as was expected, changing from one model to the other in the range of concentrations studied. Zero-shear viscosities were obtained from mechanical models also, being in good agreement with previous ones. As a result, the remarkably unusual viscoelastic profiles of exfoli-

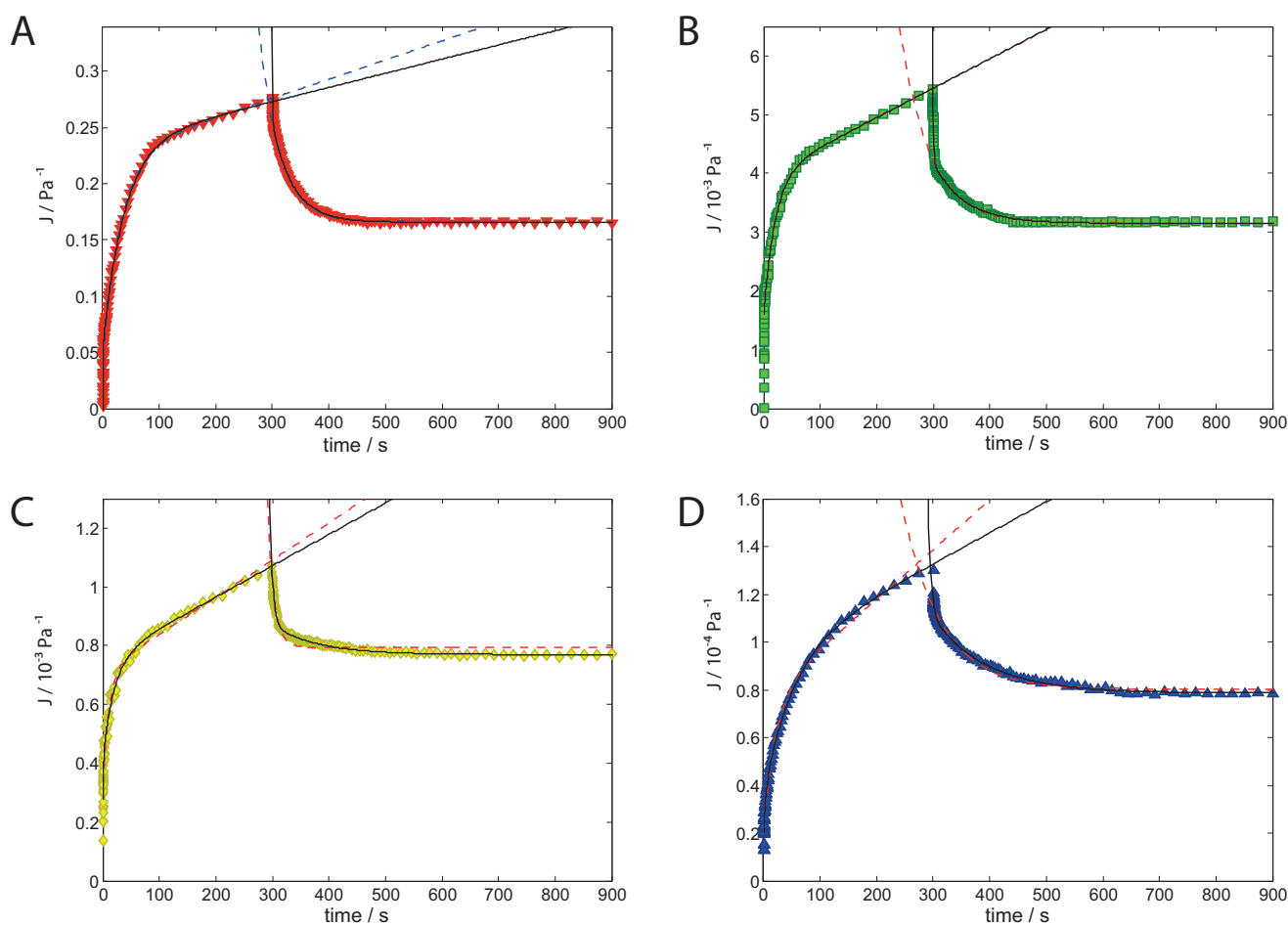


Fig. 15 Fitting of Burgers (dashed lines) and compound Voigt models (solid lines) of creep and recovery experimental curves (symbols) at 303.15 K for different weight fractions: (A) inverted triangle, 5 wt% ; (B) square, 10 wt% ; (C) diamond, 15 wt% and (D) triangle, 20 wt%. Note that all fits shown are rather accurate and, therefore, they overlap along several intervals of the experimental data, notably in the whole creep portion of 10wt% series

Table 4 Parameters of the fitting of mechanical models to experimental data sets. From left to right: weight fraction of nanoparticles (wt%), creep or recovery section (C/R), mechanical model (Burgers/compound Voight), zero-shear viscosity (μ_0), elastic moduli (G_0 , G_1 and G_2), relaxation times (λ_1 and λ_2) and Pearson correlation coefficient (R^2).

Conc. (wt%)	C/R	Model	μ_0 10 ³ (Pa s)	G_0 10 ³ (Pa)	G_1 10 ³ (Pa)	G_2 10 ³ (Pa)	λ_1 (s)	λ_2 (s)	R^2
20	C	Burgers	4821.60	44.82	18.45		22.02		0.994
		C. Voight	7716.05	49.55	17.19	64.14	50.35	4.03	0.999
	R	Burgers	3742.51		28.72		68.40		0.973
		C. Voight	3813.88		30.62	144.28	96.81	4.89	0.998
15	C	Burgers	790.51	3.10	2.57		11.22		0.983
		C. Voight	936.33	3.59	3.00	7.15	20.73	1.56	0.986
	R	Burgers	377.64		4.36		10.92		0.951
		C. Voight	389.71		5.71	9.78	4.77	80.19	0.993
10	C	Burgers	200.08	0.63	0.42		20.53		0.989
		C. Voight	200.08	7.84	0.42	0.68	20.54	0.00	0.983
	R	Burgers	95.06		0.94		51.68		0.985
		C. Voight	95.24		0.97	1.07	55.68	1.06	0.995
5	C	Burgers	5.87	0.02	0.01		31.89		0.992
		C. Voight	7.94	0.40	0.01	0.02	37.76	0.55	0.999
	R	Burgers	1.81		0.01		35.97		0.997
		C. Voight	1.81		0.01	0.05	37.54	0.93	0.998

ated graphite nanofluids must be emphasized. Internal structure is determined in this case not only by the nanometric size of the platelets, their mutual interactions, and the local partial order arrangement due to their shape. In addition, their bidimensional original nature has to be taken into account when describing the very rigid structure, which is clearly concentration dependent, and reaches a well evidenced "solid-like" plastic behaviour. Creep recovery tests have been performed for the first time for this type of nanofluids, giving an essential clue to describe the type of mechanical model that best describes the experimental rheological profile shown. Thus, despite the high heat and electric conductivities exhibited by exfoliated graphite nanofluids, the results presented now indicate that their accused viscoplastic behaviour will impose dramatic practical limitations to their use in the applications proposed so far, as flow conditions in microfluidics for instance can easily produce very large resistance to flow, contrarily to what might be expected a priori.

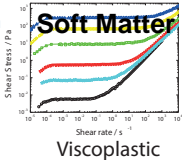
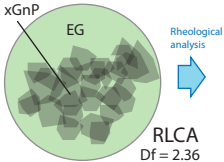
Acknowledgements

The authors thank CACTI (Univ. de Vigo) for technical assistance, M. J. Pastoriza-Gallego also thanks Xunta de Galicia for a Post-Doctoral grant.

References

- 1 K. Novoselov, A. Geim, S. Morozov, D. Jiang, Y. Zhang, S. Dubonos, I. Grigorieva and A. Firsov, *Science*, 2004, **306**, 666–669.
- 2 A. Geim and K. Novoselov, *Nature Mater.*, 2007, **6**, 183–191.
- 3 S. Stankovich, D. Dikin, G. Dommett, K. Kohlhaas, E. Zimney, E. Stach, R. Piner, S. Nguyen and R. Ruoff, *Nature*, 2006, **442**, 282–286.
- 4 A. Balandin, S. Ghosh, W. Bao, I. Calizo, D. Teweldebrhan, F. Miao and C. Lau, *Nano Lett.*, 2008, **8**, 902–907.
- 5 K. Kalaitzidou, H. Fukushima and L. Drzal, *Carbon*, 2007, **45**, 1446–1452.
- 6 M. S. Goh and M. Pumera, *Chemistry – An Asian Journal*, 2010, **5**, 2355–2357.
- 7 Y. Zhu, S. Murali, W. Cai, X. Li, J. W. Suk, J. R. Potts and R. S. Ruoff, *Adv. Mater.*, 2010, **22**, 3906–3924.
- 8 D. Chung, *J. Mat. Sci.*, 2016, **51**, 554–568.
- 9 S. U. Choi, *American Society of Mechanical Engineers, Fluids Engineering Division (Publication) FED*, 1995, **231**, 99–105.
- 10 H. Xie, W. Yu, Y. Li and L. Chen, *Proceedings of the ASME Micro/Nanoscale Heat and Mass Transfer International Conference 2009, MNHMT2009*, 2010, **1**, 591–598.
- 11 J. Buongiorno, D. Venerus, N. Prabhat, T. McKrell, J. Townsend, R. Christianson, Y. Tolmachev, P. Keblinski, L.-W. Hu, J. Alvarado, I. Bang, S. Bishnoi, M. Bonetti, F. Botz, A. Cecere, Y. Chang, G. Chen, H. Chen, S. Chung, M. Chyu, S. Das, R. Di Paola, Y. Ding, F. Dubois, G. Dzido, J. Eapen, W. Escher, D. Funfschilling, Q. Galand, J. Gao, P. Gharagozloo, K. Goodson, J. Gutierrez, H. Hong, M. Horton, K. Hwang, C. Iorio, S. Jang, A. Jarzebski, Y. Jiang, L. Jin, S. Kabelac, A. Kamath, M. Kedzierski, L. Kieng, C. Kim, J.-H. Kim, S. Kim, S. Lee, K. Leong, I. Manna, B. Michel, R. Ni, H. Patel, J. Philip, D. Poulikakos, C. Reynaud, R. Savino, P. Singh, P. Song, T. Sundararajan, E. Timo-

- feeva, T. Tritcak, A. Turanov, S. Van Vaerenbergh, D. Wen, S. Witharana, C. Yang, W.-H. Yeh, X.-Z. Zhao and S.-Q. Zhou, *J. Appl. Phys.*, 2009, **106**, 094312.
- 12 N. Prabhat, J. Buongiorno and L.-W. Hu, *ASME/JSM E 2011 8th Thermal Engineering Joint Conference, AJTEC 2011*, 2011.
- 13 A. Nasiri, M. Shariaty-Niasar, A. Rashidi and R. Khodafarin, *Int. J. Heat Mass Transfer*, 2012, **55**, 1529–1535.
- 14 J. Nanda, C. Maranville, S. Bollin, D. Sawall, H. Ohtani, J. Remillard and J. Ginder, *J. Phys. Chem. C*, 2008, **112**, 654–658.
- 15 Y. Ding, H. Alias, D. Wen and R. A. Williams, *Int. J. Heat Mass Transfer*, 2006, **49**, 240–250.
- 16 Y. Yang, Z. G. Zhang, E. A. Grulke, W. B. Anderson and G. Wu, *Int. J. Heat Mass Transfer*, 2005, **48**, 1107–1116.
- 17 S. W. Lee, K. M. Kim and I. C. Bang, *Int. J. Heat Mass Transfer*, 2013, **65**, 348–356.
- 18 W. Yu, H. Xie, X. Wang and X. Wang, *Phys. Lett. A*, 2011, **375**, 1323–1328.
- 19 A. Mariano, M. Pastoriza-Gallego, L. Lugo, L. Mussari and M. Piñeiro, *Int. J. Heat Mass Transfer*, 2015, **85**, 54–60.
- 20 M. Pastoriza-Gallego, L. Lugo, D. Cabaleiro, J. Legido and M. Piñeiro, *J. Chem. Thermodyn.*, 2014, **73**, 23–30.
- 21 M. Pastoriza-Gallego, C. Casanova, J. Legido and M. Piñeiro, *Fluid Phase Equilib.*, 2011, **300**, 188–196.
- 22 W. Tesfai, P. Singh, Y. Shatilla, M. Iqbal and A. Abdala, *J. Nanopart. Res.*, 2013, **15**:1989, 1–7.
- 23 P. Dhar, M. Ansari, S. Gupta, V. Siva, T. Pradeep, A. Pattamatta and S. Das, *J. Nanopart. Res.*, 2013, **15**:2095, 1–12.
- 24 A. Ijam, R. Saidur, P. Ganesan and A. M. Golsheikh, *Int. J. Heat Mass Transfer*, 2015, **87**, 92–103.
- 25 M. Hadadian, E. Goharshadi and A. Youssefi, *J. Nanopart. Res.*, 2014, **16**:2788, 1–17.
- 26 M. Pastoriza-Gallego, L. Lugo, J. Legido and M. Piñeiro, *Nanoscale Res. Lett.*, 2011, **6**, 1–7.
- 27 M. Pastoriza-Gallego, M. Pérez-Rodríguez, C. Gracia-Fernández and M. M. Piñeiro, *Soft Matter*, 2013, **9**, 11690–11698.
- 28 D. Cabaleiro, M. Pastoriza-Gallego, C. Gracia-Fernández, M. Piñeiro and L. Lugo, *Nanoscale Res. Lett.*, 2013, **8**, 1.
- 29 M. Mehrali, E. Sadeghinezhad, S. Latibari, S. Kazi, M. Mehrali, M. Zubir and H. Metselaar, *Nanoscale Res. Lett.*, 2014, **9**:15, 1–12.
- 30 H. Barnes and K. Walters, *Rheol. Acta*, 1985, **24**, 323–326.
- 31 H. Barnes, *J. Nonnewton. Fluid Mech.*, 1999, **81**, 133–178.
- 32 D.-H. Cheng, *Rheol. Acta*, 1986, **25**, 542–554.
- 33 P. Möller, J. Mewis and D. Bonn, *Soft Matter*, 2006, **2**, 274–283.
- 34 H. Emady, M. Caggioni and P. Spicer, *J. Rheol.*, 2013, **57**, 1761–1772.
- 35 N. Q. Dzuy and D. Boger, *J. Rheol.*, 1983, **27**, 321–349.
- 36 L. Zhu, N. Sun, K. Papadopoulos and D. De Kee, *J. Rheol.*, 2001, **45**, 1105–1122.
- 37 M. Balhoff, L. Lake, P. Bommer, R. Lewis, M. Weber and J. Calderin, *J. Petrol. Sci. Eng.*, 2011, **77**, 393–402.
- 38 R. Larson, *J. Rheol.*, 2005, **49**, 1–70.
- 39 Z. Xu and C. Gao, *Nat Commun.*, 2011, **2**, 571.
- 40 G. Vradis and M. Ötügen, *J. Fluids Eng., Transactions of the ASME*, 1997, **119**, 193–200.
- 41 A. Ahmed and A. N. Alexandrou, *American Society of Mechanical Engineers, Fluids Engineering Division (Publication) FED*, 1994, **179**, 83–87.
- 42 E. C. Bingham, *Fluidity and Plasticity*, McGraw-Hill Book Company, Incorporated, 1922, vol. 2.
- 43 W. Herschel and R. Bulkley, *Kolloid-Zeitschrift*, 1926, **39**, 291–300.
- 44 T. C. Papanastasiou, *J. Rheol.*, 1987, **31**, 385–404.
- 45 Q.-H. Nguyen and N.-D. Nguyen, in *Incompressible Non-Newtonian Fluid Flows*, ed. D. Y. Gan, InTech, 2012, ch. 3.
- 46 J. Guo and J. Lewis, *J. Am. Ceram. Soc.*, 2000, **83**, 266–272.
- 47 C. Allain, M. Cloitre and M. Wafra, *Phys. Rev. Lett.*, 1995, **74**, 1478–1481.
- 48 W. Shih, W.-H. Shih and I. Aksay, *J. Am. Ceram. Soc.*, 1999, **82**, 616–624.
- 49 W. Tseng and K.-C. Lin, *Mater. Sci. Eng., A*, 2003, **355**, 186–192.
- 50 M. Lin, H. Lindsay, D. Weitz, R. Klein, R. Ball and P. Meakin, *J. Physics: Cond. Matter*, 1990, **2**, 3093–3113.
- 51 M. Ojovan and W. Lee, *J. Phys: Condens. Matter*, 2006, **18**, 11507–11520.
- 52 N. Marcovich, M. Auad, N. Bellesi, S. Nutt and M. Aranguren, *J. Mater. Res.*, 2006, **21**, 870–881.
- 53 J. Steffe, *Rheological Methods in Food Process Engineering*, Freeman Press: New York, 1996.
- 54 T. G. Mezger, *The Rheology Handbook*, Vincentz Network: Hannover, 2nd edn., 2006.
- 55 F. Mainardi, *Fractional Calculus and Waves in Linear viscoelasticity: An Introduction to Mathematical Models*, Imperial College Press: London, 2010.



Mechanical model

